

1 **Direct observation of core-shell structure and water**
2 **uptake of individual submicron urban aerosol particles**

3 Ruiqi Man¹, Yishu Zhu^{1,†}, Zhijun Wu^{1,2,*}, Peter Aaron Alpert^{3,‡}, Bingbing Wang⁴, Jing
4 Dou^{5,§}, Jie Chen⁵, Yan Zheng¹, Yanli Ge¹, Qi Chen¹, Shiyi Chen¹, Xiangrui Kong⁶,
5 Markus Ammann³, Min Hu¹

6 ¹State Key Joint Laboratory of Environmental Simulation and Pollution Control, College of
7 Environmental Sciences and Engineering, Peking University, Beijing, 100871, China

8 ²Collaborative Innovation Center of Atmospheric Environment and Equipment Technology, Nanjing
9 University of Information Science and Technology, Nanjing, 210044, China

10 ³Laboratory of Atmospheric Chemistry, PSI Center for Energy and Environmental Sciences, Paul
11 Scherrer Institute, Villigen, 5234, Switzerland

12 ⁴College of Ocean and Earth Sciences, State Key Laboratory of Marine Environmental Science,
13 Xiamen University, Xiamen, 361102, China

14 ⁵Institute for Atmospheric and Climate Science, ETH Zürich, Zürich, 8092, Switzerland

15 ⁶Department of Chemistry and Molecular Biology, University of Gothenburg, Gothenburg, 41390,
16 Sweden

17 [†]now at Department of Earth and Planetary Science, University of California Berkeley, Berkeley, CA,
18 94720, USA

19 [‡]now at XRnanotech GmbH, Parkstrasse 1, Villigen, 5234, Switzerland

20 [§]now at Institute for Atmospheric and Earth System Research, University of Helsinki, Helsinki, 00014,
21 Finland

22 *Correspondence to: Zhijun Wu (zhijunwu@pku.edu.cn)

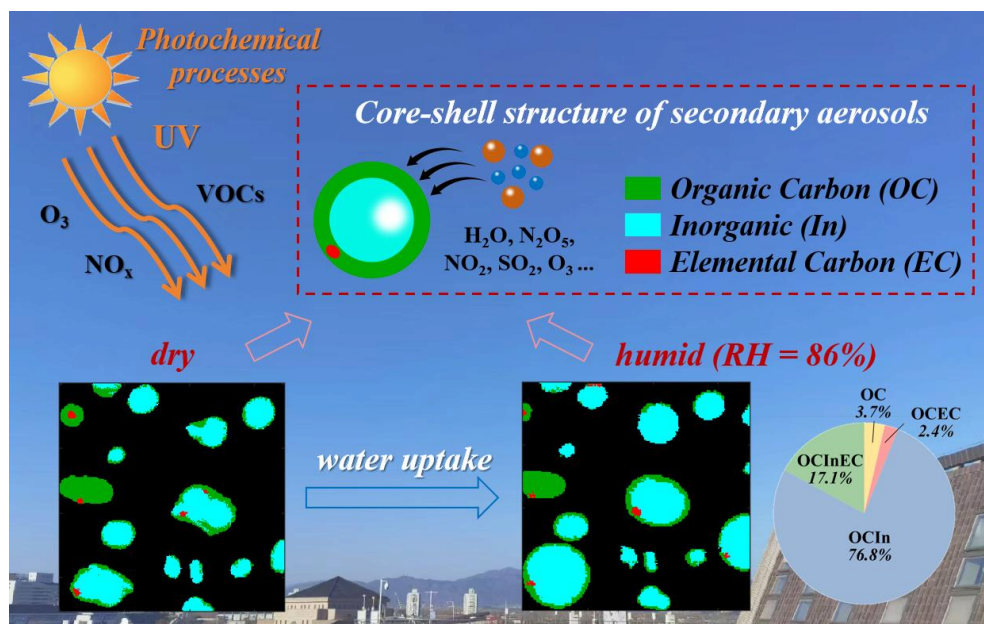
23 **Abstract.** Determining the particle chemical morphology is crucial for unraveling reactive uptake in
24 atmospheric multiphase and heterogeneous chemistry. However, it remains challenging due to the
25 complexity and inhomogeneity of aerosols particles. Using a scanning transmission X-ray microscopy
26 (STXM) coupled with near-edge X-ray absorption fine structure (NEXAFS) spectroscopy and an
27 environmental cell, we imaged and quantified the chemical morphology and hygroscopic behavior of
28 individual submicron urban aerosol particles. Results show that internally mixed particles composed of
29 organic carbon and inorganic matter (OCIn) dominated the particle population ($73.1 \pm 7.4\%$). At 86%
30 relative humidity, 41.6% of the particles took up water, with OCIn particles constituting 76.8% of these
31 hygroscopic particles. Most particles exhibited a core-shell structure under both dry and humid
32 conditions, with an inorganic core and an organic shell. Our findings provide direct observational

33 evidence of the core-shell structure and water uptake behavior of typical urban aerosols, which
34 underscore the importance of incorporating the core-shell structure into models for predicting the
35 reactive uptake coefficient of heterogeneous reactions.

36 **Short summary:** The particle chemical morphology is important to atmospheric multiphase and
37 heterogeneous chemistry. This work directly observed the core-shell structure and water uptake
38 behavior of individual submicron aerosol particles at an urban site and elucidated the potential impact
39 on particle reactive uptake and heterogeneous reactions.

40 **Keywords:** urban air pollution; individual particles; chemical morphology; core-shell structure; water
41 uptake

42 **Table of Contents Graphic:**



43

44 **1 Introduction**

45 Aerosols have significant impacts on visibility, climate, and human health (McCormick and
46 Ludwig, 1967; Noll et al., 1968; Chow et al., 2006; Rasool and Schneider, 1971). As particles in the
47 atmosphere usually act as reaction vessels for various reactions, the physicochemical properties of
48 aerosol particles play an important role in reactive uptake of gaseous molecules onto particles, mass
49 transfer and gas-particle partitioning equilibrium, and transformation mechanisms of pollutants (Abbatt
50 et al., 2012; Davidovits et al., 2011; George et al., 2015; George and Abbatt, 2010; Su et al., 2020;
51 Ziemann and Atkinson, 2012). Therefore, quantitatively characterizing the aerosol physicochemical
52 properties is vital to atmospheric multiphase and heterogeneous chemistry (Freedman, 2017; Li et al.,
53 2016; Riemer et al., 2019; Tang et al., 2016).

54 The aerosol physicochemical properties, such as the particle size, chemical morphology (defined
55 as the spatial distribution of various chemical components within a particle herein), mixing state, and
56 hygroscopicity vary under different ambient conditions. These properties and their variations have a
57 critical influence on reactive uptake, a key process in multiphase chemistry which is initiated by the
58 collision of a gas-phase reactant with a condensed-phase surface (Davies and Wilson, 2018; Reynolds
59 and Wilson, 2025). Organic coatings of particles with core-shell structures inhibit reactive uptake of
60 dinitrogen pentoxide (N_2O_5) by particulate matter by means of affecting mass accommodation, the
61 availability of water for hydrolysis, and mass transport (Wagner et al., 2013; Jahl et al., 2021; Jahn et
62 al., 2021). Without considering the core-shell structure, the reactive uptake coefficient of N_2O_5 tends to
63 be overestimated from several times to tens of times (Wagner et al., 2013). Therefore, investigating the
64 particle chemical morphology is necessary for accurately quantifying the uptake coefficient and
65 reducing uncertainty in heterogeneous reactions.

66 So far, extensive research has been conducted on the physicochemical properties of bulk aerosols
67 by various techniques, such as the Humidified Tandem Differential Mobility Analyzer (H-TDMA),
68 Aerosol Mass Spectrometer (AMS), and Soot Particle Aerosol Mass Spectrometer (SP-AMS) (Li et al.,
69 2016; Tang et al., 2019; Riemer et al., 2019). However, the bulk analysis mostly obtains indirect
70 information about the physicochemical properties of particle populations based on assumptions and
71 estimations, which is difficult to directly observe the chemical morphology and mixing state of aerosol
72 particles (Li et al., 2016). This knowledge gap hinders our understanding of the role of aerosol particles

73 in reactive uptake and heterogeneous processes. As a comparison, individual particle analysis can
74 provide direct observational evidence about the chemical morphology and mixing state at the
75 microscopic scale, which is essential for exploring particle hygroscopic and optical properties (Krieger
76 et al., 2012; Li et al., 2016; Posfar et al., 2010; Wu and Ro, 2020).

77 Scanning transmission X-ray microscopy combined with near-edge X-ray absorption fine
78 structure (STXM/NEXAFS) spectroscopy bases on synchrotron radiation technology. It is a robust
79 technique for obtaining chemical morphology information of numerous individual particles with high
80 spectral energy resolution and chemical specificity, as it can identify and distinguish various chemical
81 composition at the single particle level within a particle population (Moffet et al., 2011; Shao et al.,
82 2022). The soft X-ray energy range of STXM (100 – 2000 eV for STXM versus 50 – 200 keV for
83 electron microscopy) makes it possible to quantify light elements (such as carbon, nitrogen, and
84 oxygen) with little beam damage (Moffet et al., 2011). In addition, STXM doesn't require ultrahigh
85 vacuum conditions (Moffet et al., 2011). In short, STXM/NEXAFS spectroscopy provides an enhanced
86 chemical sensitivity for obtaining specific organic chemical bonds, functional groups, and speciation
87 information, which has enormous potential in exploring ambient samples under atmospheric relevant
88 conditions, especially submicron-sized particles.

89 Compared with other STXM endstations which generally analyze samples under vacuum
90 conditions (Alpert et al., 2022; Bondy et al., 2018; Fraund et al., 2020; Knopf et al., 2023; Lata et al.,
91 2021; Moffet et al., 2010a; Moffet et al., 2010b; Moffet et al., 2013; Moffet et al., 2016; Tomlin et al.,
92 2022), several STXM instruments are equipped with an in-situ temperature and relative humidity (RH)
93 control environmental cell, allowing for investigating hygroscopicity and water uptake behavior of
94 laboratory-generated particles (Ghorai and Tivanski, 2010; O'brien et al., 2015; Piens et al., 2016;
95 Zelenay et al., 2011a; Zelenay et al., 2011b). However, only a few researches focusing on hygroscopic
96 behavior of ambient particles has been reported so far, and these particles were collected in rural
97 environment (Piens et al., 2016) or forest (Mikhailov et al., 2015; Pöhlker et al., 2014). Studies on
98 water uptake of urban aerosol particles using STXM and corresponding knowledge for their chemical
99 morphology under humid conditions is currently lacking.

100 In recent years, the air quality in China has improved notably due to the implementation of a
101 series of strict pollution mitigation measures. These improvements are attributed to decreasing primary
102 emissions, while the contributions of secondary species to particle mass have become more significant

103 (Lei et al., 2021; Wang et al., 2019). To elucidate the causes and mechanisms of pollution episodes in
104 China, numerous research has been carried out on the pollution characteristics (Gao et al., 2015; Gao et
105 al., 2018; Guo et al., 2014; Huang et al., 2014; Liu et al., 2018; Sun et al., 2013; Wang et al., 2014;
106 Zhao et al., 2013) and physicochemical properties (Gao and Anderson, 2001; Li et al., 2017; Shen et al.,
107 2019; Song et al., 2022) of ambient aerosols. However, there is still a lack of study on direct
108 observation of the chemical morphology and hygroscopic behavior of secondary urban aerosols at the
109 single particle level. This knowledge gap hinders our understanding of the role of secondary aerosols as
110 reaction vessels in heterogeneous reactions.

111 In this study, we investigated the chemical morphology of ambient individual submicron aerosol
112 particles using STXM/NEXAFS spectroscopy. The ambient samples were collected at an urban site in
113 North China Plain, Beijing during a pollution episode. We also explored the chemical morphology and
114 water uptake behavior of individual particles at high humidity (RH = 86%) using an environmental cell.
115 This work aims to improve our comprehension of the physicochemical properties of particles in typical
116 urban pollution atmospheres, aiding in clarifying their atmospheric heterogeneous processes and
117 multiphase chemistry.

118 **2 Materials and methods**

119 **2.1 Sampling and instruments**

120 To study the physicochemical properties of ambient particles, samples were collected during a
121 pollution episode at the Peking University Urban Atmosphere Environment Monitoring Station
122 (PKUERS, 39°59'21"N, 116°18'25"E) in Beijing, China. More details about the measurement site can
123 be found in our previous studies (Tang et al., 2021; Wu et al., 2007).

124 The individual particle sample was collected using a four-stage cascade impactor with a Leland
125 Legacy personal sample pump (Sioutas, SKC, Inc., the US) at a flow rate of 9 L min⁻¹. The sampling
126 started at 5:04 P.M. on October 1st, 2019 and lasted for 5 minutes. The sampling substrate was a copper
127 grid (Lacey Carbon 200 mesh, Ted Pella, Inc., the US) suitable for its X-ray transparency. Particles
128 collected onto the last stage with the 50% cut-point aerodynamic diameter of 250-nm were used for
129 STXM analysis. The sample was placed into a sample box sealed with a bag filled with nitrogen, and it
130 was stored in a freezer at a temperature of -18°C until analysis. Previous results indicate that the

131 chemical composition of organic aerosols (especially secondary organic aerosols, SOA) and the mass
132 concentrations of black carbon (BC) both remained stable for several weeks under low-temperature
133 storage conditions (-20°C and -80°C for organic aerosols, and 2°C , 4°C , and 5°C for BC); while
134 significant changes occurred over time when samples were stored at room temperature even just for a
135 few days (Mori et al., 2016; Mori et al., 2019; Resch et al., 2023; Ueda et al., 2025; Wendl et al.,
136 2014).

137 Other parameters were measured from September 28th to October 7th, 2019. The non-refractory
138 chemical composition of submicron particles (NR-PM₁) was obtained by a Long Time-of-Flight
139 Aerosol Mass Spectrometer (LTOF-AMS, Aerodyne Research Inc., the US) (Zheng et al., 2020; Zheng
140 et al., 2023). Calibrations of ionization efficiency (IE) and relative IE followed the standard procedures
141 described in previous studies (Canagaratna et al., 2007; Fröhlich et al., 2013). The reference
142 temperature and pressure conditions of mass concentrations reported herein were 293.7 K and 101.82
143 KPa. We applied composition-dependent collection efficiency (CDCE) values (0.50 ± 0.01 , mean \pm
144 standard deviation) that were calculated by the methods introduced by Middlebrook et al. (2012) to the
145 AMS data. The mass concentration of fine particles (PM_{2.5}) was measured by a TEOM analyzer
146 (TH-2000Z1, Wuhan Tianhong Environmental Protection Industry Co., Ltd., China). Meteorological
147 parameters including temperature (T), RH, wind speed, and wind direction were monitored by an
148 integrated 5-parameter Weather Station (MSO, Met One Instruments, Inc., the US).

149 **2.2 STXM/NEXAFS analysis**

150 In order to gain the chemical morphology, mixing state, and component information of individual
151 particles, STXM/NEXAFS spectroscopy measurements were carried out at the PolLux beamline
152 (X07DA) of the Swiss Light Source (SLS) at Paul Scherrer Institute (PSI) (Raabe et al., 2008). In brief,
153 X-rays illuminated a Fresnel zone plate focusing the beam to a pixel of $35 \times 35 \text{ nm}^2$. The zone plate has
154 a central stop that acts together with another optic known as an order sorting aperture to eliminate
155 unfocused and higher-order light, ensuring only first-order focused light is transmitted to the sample.
156 Then, X-rays transmitted through the sample are detected. The absorbance of each pixel is
157 characterized by optical density (OD) based on the Beer-Lambert's law as follows,

$$\text{OD} = -\ln (I/I_0) \quad (1)$$

158 where I and I_0 are the intensity of photons transmitted through a sample region and a sample-free
159 region, respectively. Further details including the uncertainty estimation of OD are described in the
160 Supplementary Information (SI).

161 STXM/NEXAFS spectroscopy scans X-ray energies over particles with high spectral energy
162 resolution. When inner shell electrons of atoms absorb X-ray photons, they can transition into
163 unoccupied valence orbitals, resulting in an absorption peak that is used to identify specific bonding
164 characteristics. The amount of absorption depends on the photon energy (E), elemental composition, as
165 well as sample thickness and density (Moffet et al., 2011). We employed two measurement strategies
166 to optimize photon flux to the particles, achieving the best signal-to-noise ratio while minimizing the
167 scan time. The first strategy was a high energy-resolution mode with an X-ray energy resolution $\Delta E =$
168 0.2 eV and a coarse pixel size of around $100 \times 100 \text{ nm}^2$ to measure absorption at small energy steps.
169 The energy resolution is defined as being able to distinguish between two absorption peaks separated
170 by ΔE at the full width at half maximum OD. In this mode, carbon (C), nitrogen (N), and oxygen (O)
171 K-edge spectra of individual particles were measured. The energy offset of C and O spectra were +0.4
172 eV and +1.2 eV respectively, according to the energy calibration procedures using polystyrene spheres
173 and gas-phase carbon dioxide (CO₂). The energy offset of N at the K-edge was not calibrated, however,
174 the obtained spectra of ambient particles appeared identical to ammonium salts in literature (Ekimova
175 et al., 2017; Latham et al., 2017). Due to the presence of ammonium, which was confirmed in particles
176 using AMS, we applied a calibration factor of +0.1 eV for the N K-edge to match our observed main
177 peak to that of ammonium at 405.7 eV. Optical density detected over the same spot at different photon
178 energies at the carbon and nitrogen K-edges was displayed in Fig. S1, and less beam damage during the
179 experiment was confirmed.

180 The second strategy is a high spatial-resolution mode with a pixel size of $35 \times 35 \text{ nm}^2$ and $\Delta E =$
181 0.6 eV, where imaged at four specific energies for the C K-edge, namely, 278.0 eV, 285.4 eV, 288.6
182 eV, and 320.0 eV. Automated analysis followed the methodology of Moffet et al. (2010a) and Moffet
183 et al. (2016). In brief, absorption at 278.0 eV ($\text{OD}_{278.0\text{eV}}$) is regarded as the pre-edge of carbon, which is
184 mainly due to off-resonance absorption by inorganic elements other than carbon. Absorption at 285.4
185 eV ($\text{OD}_{285.4\text{eV}}$) is due to the characteristic transition of sp^2 hybridized carbon (i.e., doubly bonded
186 carbon). Since this peak is abundant for elemental carbon (EC), it can be used to discern soot, because
187 EC is a type of components of soot (Penner and Novakov, 1996). Absorption at 288.5 eV ($\text{OD}_{288.5\text{eV}}$)

188 comes from carboxylic carbonyl groups, which are common in organic aerosols in atmospheres.
189 Therefore, organic carbon (OC) is identified by this energy. Absorption of the post-edge at 320.0 eV
190 ($OD_{320.0\text{eV}}$) is contributed by carbonaceous and non-carbonaceous atoms (Moffet et al., 2010a).

191 Based on absorption at these four typical energies, we obtain three images by further processing.
192 The difference between OD at the post-edge and OD at the pre-edge ($OD_{320.0\text{eV}} - OD_{278.0\text{eV}}$) indicates
193 total carbon. The ratio of OD at the pre-edge to OD at the post-edge ($OD_{278.0\text{eV}} / OD_{320.0\text{eV}}$) indicates the
194 relative absorption contribution of inorganic matter (In). Compared with the absorbance contribution of
195 doubly bonded carbon to total carbon (% sp^2) in the highly oriented polycrystalline graphite (HOPG,
196 assuming that % $sp^2 = 100\%$) at 285.4 eV, the spatial distribution of EC/soot in samples can be
197 identified by the procedure of Hopkins et al. (2007). It is assumed that total carbon consists of OC and
198 EC. The thresholds of these images follow the criteria mentioned in Moffet et al. (2010a) and Moffet et
199 al. (2016). These three images described above were then overlaid to create a chemical map of
200 individual particles.

201 **2.3 Criterion of particle water uptake based on the total oxygen absorbance**

202 To determine whether particles took up water, a criterion was established on the basis of the total
203 oxygen absorbance determined at the energy of 525.0 eV (the pre-edge of oxygen) and 550.0 eV (the
204 post-edge of oxygen). Based on the same principle as the total carbon calculation, the difference
205 between OD at the post-edge and pre-edge of oxygen represents the total oxygen absorbance. Due to
206 the fact that each particle is composed of some pixels, the total oxygen absorbance (ΔOD) of an
207 individual particle under dry and humid conditions is calculated as follows,

$$\Delta OD_{dry} = \sum_{i=1}^m \Delta OD_i = \sum_{i=1}^m (OD_{post,i} - OD_{pre,i}) = \sum_{i=1}^m OD_{post,i} - \sum_{i=1}^m OD_{pre,i} \quad (2)$$

$$\Delta OD_{humid} = \sum_{j=1}^n \Delta OD_j = \sum_{j=1}^n (OD_{post,j} - OD_{pre,j}) = \sum_{j=1}^n OD_{post,j} - \sum_{j=1}^n OD_{pre,j} \quad (3)$$

208 where m and n are numbers of pixels that make up an individual particle under dry and humid
209 conditions, i and j are a certain pixel within an individual particle under dry and humid conditions, *post*
210 and *pre* respectively represent the energy at the post-edge (550.0 eV) and that at the pre-edge (525.0 eV)
211 of oxygen. If a particle takes up water, the amount of oxygen atoms within this particle will increase,
212 leading to an amplification in ΔOD . Water uptake may increase particle height and absorption. On the

213 other hand, it possibly causes a particle to spread out, which may reduce particle height and thus
214 absorption. Although a thinner particle that contains more water may result in less absorption at some
215 specific pixels, ΔOD_{humid} will be larger than ΔOD_{dry} due to the fact that more pixels are summed, i.e.,
216 $n > m$. Therefore, comparing the results of Eq. 2 and Eq. 3 will quantify the total oxygen absorbance of
217 a particle under dry and humid conditions, and determine particle water uptake. Specifically, if
218 $\Delta OD_{humid} > \Delta OD_{dry}$, then we assume that a particle has taken up water.

219 **2.4 A novel in-situ environmental cell**

220 To explore the chemical morphology and hygroscopicity of the particles under humid conditions,
221 we adjusted the RH of an in-situ environmental cell with sample placed in it. The environmental cell
222 can also be used for trace gas reactive uptake and photochemical reactions with laboratory-generated
223 particles (Alpert et al., 2019; Alpert et al., 2021). The environmental cell used in this study consists of a
224 removable sample clip that hosts a sealed silicon nitride (SiNit) window and a main body that contains
225 gas supply lines and temperature control. Together, they are mounted in the STXM vacuum chamber.
226 A SiNit window at the back side of the main body is also sealed and ensures X-ray transparency
227 passing through the whole environmental cell assembly. Descriptions of the connections for the gas
228 supply, heating and cooling devices, and temperature measurement can be found in previous studies
229 (Huthwelker et al., 2010; Zelenay et al., 2011a). The detailed methods of collecting the ambient
230 particles by the impactor and measuring them in the environmental cell were shown in the SI.

231 We performed humidity calibration experiments to make sure sufficient heat transfer and a
232 homogeneous water vapor field across the samples. It is important due to the fact that the only way for
233 samples to gain or lose heat and water was through air contact. To study the accuracy of RH in the
234 environmental cell, water uptake and deliquescence of a sodium chloride (NaCl) standard sample was
235 observed. The deliquescence relative humidity (DRH) of pure NaCl crystals obtained from literature
236 and thermodynamic models is around 75 – 76% at room temperature (Eom et al., 2014; Martin, 2000;
237 Peng et al., 2022). The images of the NaCl sample displayed in Fig. S2 illustrate the morphological
238 changes as RH increased. As shown in Fig. S2, particle morphologies in panels (A) – (C) remained
239 essentially identical before RH reached the DRH of NaCl, although the focus position slightly varied in
240 different panels. When RH was 75.6% (Fig. S2D), particles completely deliquesced and some
241 coalesced. The uncertainty of RH in the environmental cell in this study was determined conservatively

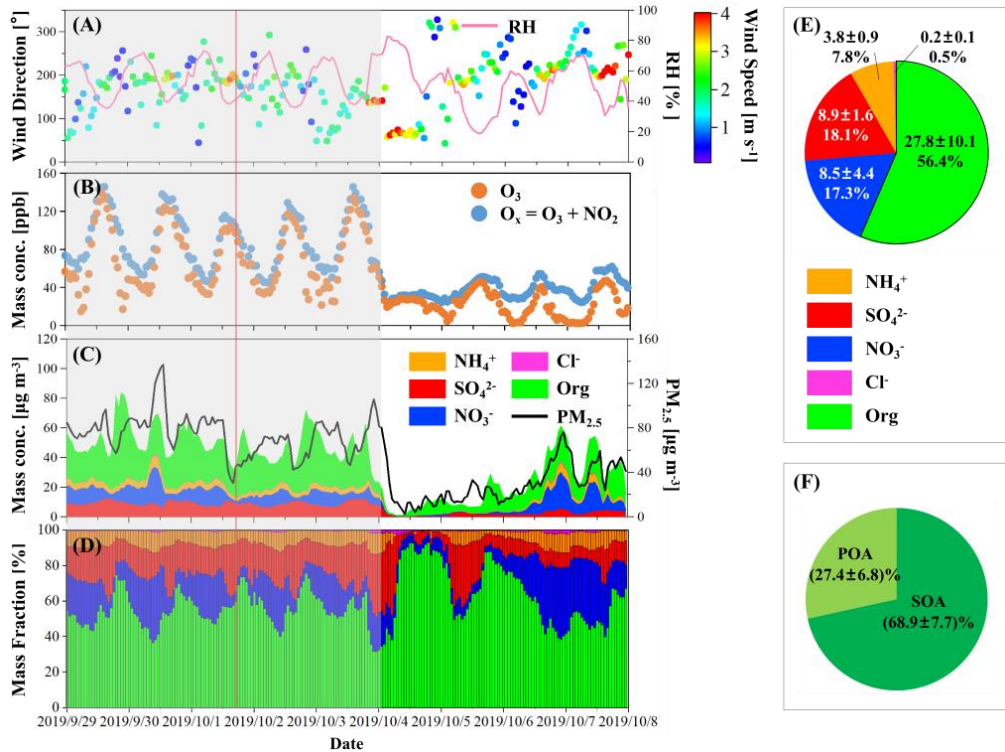
242 to be $\pm 2\%$, in agreement with previous results (Huthwelker et al., 2010). Information about the oxygen
243 K-edge spectra of the NaCl sample at high RH can be found in Fig. S3.

244 **3 Results and discussion**

245 **3.1 Pollution characteristics during the sampling period**

246 Time series of meteorological parameters, mass concentrations of gaseous pollutants, PM_{2.5}, and
247 NR-PM₁ are shown in Fig. 1. During the pollution episode from September 29th to October 3rd, 2019,
248 the stagnant weather condition with low wind speed led to pollution accumulation. The air became
249 clean due to the appearance of a strong north wind on October 4th (Fig. 1A). The sampling time of the
250 individual particle sample was 5:04 P.M. on October 1st (see the red line in Fig. 1) with an ozone (O₃)
251 concentration of 97.1 ppb. The average mass fractions of chemical composition of NR-PM₁ during the
252 sampling period of individual particles could be found in Fig. S4. During this period, the low mass
253 fraction of volatile inorganic species such as nitrate made it suitable for measurements using offline
254 techniques, such as STXM, because the loss of volatile species during storage and measurement
255 processes was minimal.

256 During the pollution episode, the maximum daily 8-hour average of ozone (MDA8-O₃) was 110.3
257 ± 10.1 ppb (i.e., $236.5 \pm 21.7 \mu\text{g m}^{-3}$). The concentration of O_x [O_x = nitrogen dioxide (NO₂) + O₃] was
258 88.6 ± 29.4 ppb (Fig. 1B), reflecting a high atmospheric oxidation capacity that drives secondary
259 transformations of gaseous pollutants (Dou et al., 2024; Xiao et al., 2022). The average PM_{2.5} was $74.3 \pm 18.3 \mu\text{g m}^{-3}$ (Fig. 1C). As shown in Fig. 1D – 1E, the average mass concentration of secondary
261 inorganic aerosol (SIA) in NR-PM₁ was $21.3 \pm 4.8 \mu\text{g m}^{-3}$, with sulfate and nitrate contributing almost
262 equally to particle mass (i.e., 18.1% and 17.3% respectively). Organic matter in NR-PM₁ had an
263 average mass fraction of 56.4% (Fig. 1E). The mass concentrations of primary organic aerosol (POA)
264 and SOA were estimated based on the positive matrix factorization (PMF) analysis (Ulbrich et al.,
265 2009). As shown in Fig. 1F, SOA dominated organic matter, contributing an average of 68.9%. Overall,
266 this pollution episode was led by secondary oxidation processes and featured by high contributions of
267 secondary particulate species.



268

269 **Figure 1:** Time series of (A) wind direction, wind speed, and relative humidity (RH), (B) mass
 270 concentrations of ozone (O₃) and O_x (O₃ + nitrogen dioxide, NO₂), (C) mass concentrations of fine particles
 271 (PM_{2.5}) and non-refractory submicron particles (NR-PM₁), and (D) mass fractions of chemical composition
 272 of NR-PM₁ are shown. The gray area represents the pollution episode lasting from September 29th to
 273 October 3rd. The red line indicates the sampling time for the individual particle sample. (E) Pie chart
 274 showing the average mass fractions of chemical composition of NR-PM₁ during the pollution period. The
 275 number in the first row of each part is the average mass concentration and standard deviation (SD) with a
 276 unit of µg m⁻³. The number in the second row is the average mass fraction. (F) Pie chart showing the
 277 average mass contributions of primary organic aerosol (POA, light green) and secondary organic aerosol
 278 (SOA, dark green) to the total organic. Average mass fraction and SD are marked in the pie chart.

279 3.2 Chemical maps of individual particles

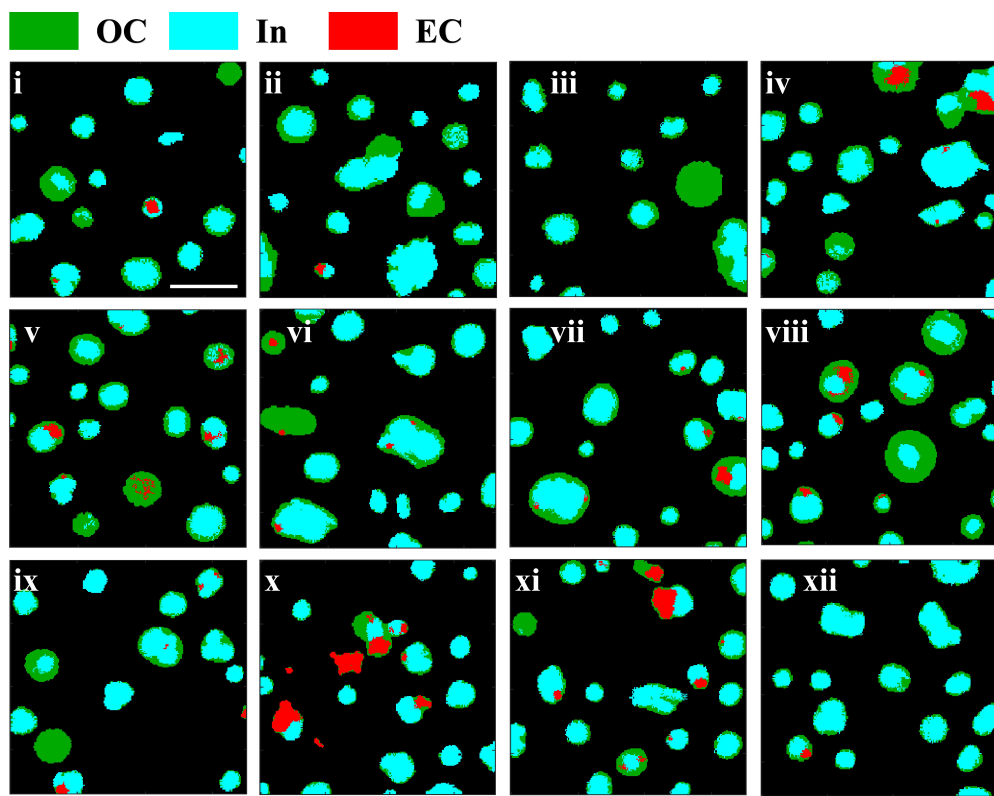
280 Chemical maps of individual particles under dry conditions are displayed in Fig. 2. Different
 281 images denote particles located in different regions of interest (ROI, 12 in total) of the sampling
 282 substrate. 197 individual particles were investigated in total. The detailed images of total carbon,
 283 inorganic, and doubly bonded carbon maps are available in Fig. S5 – S7. Most submicron particles on
 284 the substrate were round or nearly round, while supermicron particles predominantly exhibited
 285 irregular shapes. The circular equivalent diameter of individual particles was calculated, with the
 286 methods detailed in the SI. The normalized size distribution of overall particles followed a normal
 287 distribution, with a mean diameter ± standard deviation (SD) being 0.83 ± 0.30 µm (Fig. S8A). A
 288 significant proportion of the particles were within the 0.4 – 1.2 µm size range.

289 As displayed in Fig. 2, chemical maps of individual particles showed that they were dominated by
290 inorganic substances (colored in cyan), which were likely sulfate that was frequently observed by AMS
291 (Fig. 1C). Approximately one quarter (24.9%) of the particles contained EC/soot (colored in red).
292 Notably, around 82% of these soot-containing particles had soot located at particle edges. One of the
293 possible reasons is that inorganic species (such as crystals) pushed soot away from the center of the
294 particles during their efflorescence (Moffet et al., 2016). While, it should be noted that particle
295 deformation may occur during the particle collection process due to the high particle impaction
296 velocity of the impactor (O'Brien et al., 2014). Therefore, the distribution of chemical components
297 within individual particles displayed in the images may differ from that of aerosol particles in ambient
298 atmospheres. Additionally, several particles contained multiple soot components, which was also
299 observed before (Moffet et al., 2016).

300 Typically, inorganic components and/or soot were encased in organic matter, forming a core-shell
301 structure characterized by an inorganic-dominated core and an organic-dominated shell. Figure 2
302 illustrates that most organic-inorganic internally mixed particles exhibited thin coatings, likely from
303 fresh emissions. Conversely, a few particles have thick coatings, which is indicative of aging processes
304 in a highly active photochemical environment. Previous studies suggest that most of the
305 soot-containing particles with thin coatings would have rather smaller absorption enhancement
306 compared with those with thick coatings (Bond et al., 2006; Moffet et al., 2016).

307 The observed core-shell morphology could also result from liquid-liquid phase separation (LLPS),
308 influenced by fluctuating ambient RH (Fig. 1A) and determined by the oxygen-to-carbon (O:C) ratio of
309 the organic fraction (Freedman, 2020; Li et al., 2021; You et al., 2012; You et al., 2014; Freedman,
310 2017). To test this hypothesis, the O:C ratio of the individual particles composed of pure organic
311 composition was estimated as 0.53 ± 0.15 based on the STXM data. The estimation methods were
312 displayed in the SI. This falls within the threshold range for LLPS occurrence in ammonium sulfate -
313 organic mixing particles ($0 < \text{O:C} < 0.57$) (You et al., 2013). For comparison, the value of the O:C ratio
314 by AMS during the individual particle collection period is also calculated (0.60 ± 0.01), and the data
315 set was displayed in the SI. The difference between the O:C ratio results by STXM and LToF-AMS
316 may be due to the reasons as follows: (1) STXM measures individual particles, while AMS targets bulk
317 aerosols; (2) Particles collected onto the last stage using a four-stage cascade impactor with the 50%

318 cut-point aerodynamic diameter of 250-nm were used for STXM analysis, while AMS measured the
319 non-refractory chemical composition of submicron particles.



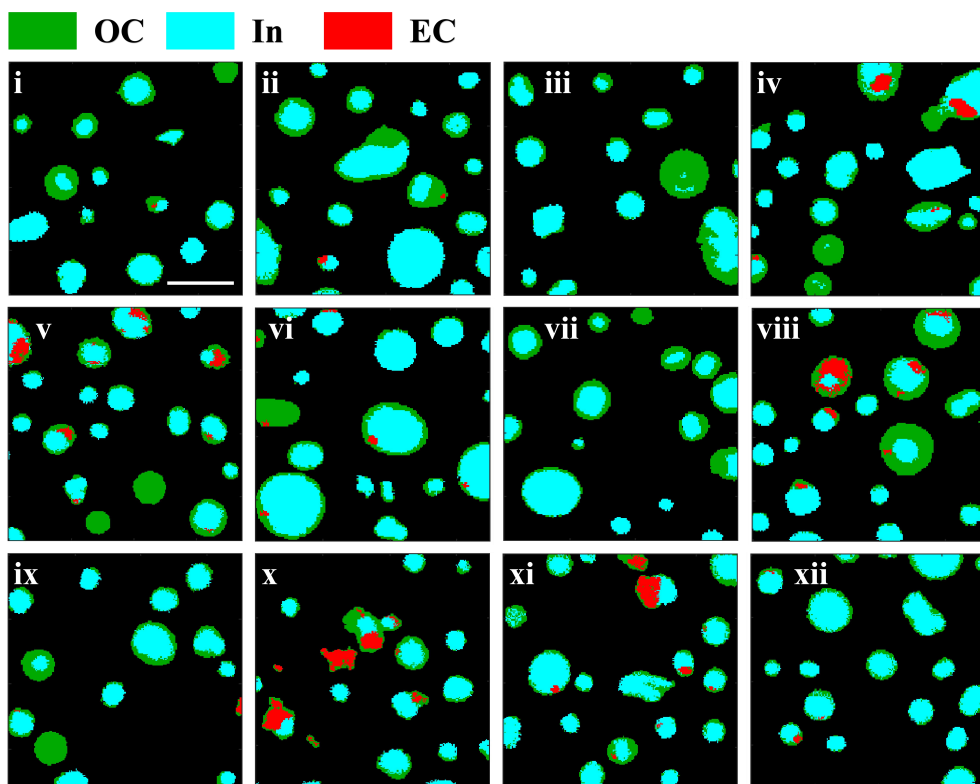
320
321 **Figure 2: Chemical maps of individual particles in 12 regions of interest (ROI) of sampling substrate under**
322 **dry conditions on the basis of pixels. Green, cyan, and red color represent dominant components of organic**
323 **carbon (OC), inorganic matter (In), and elemental carbon (EC), respectively. The scale bar in the upper left**
324 **image represents 2 μ m and applies to all the images.**

325 Statistically, the particles were categorized into four types based on their mixing state, including
326 pure organic (OC), organic internally mixed with soot (OCEC), organic internally mixed with
327 inorganic (OCIn), and organic internally mixed with inorganic and soot (OCInEC). OCIn particles
328 were the most abundant type in the examined particle population ($73.1 \pm 7.4\%$), followed by OCInEC
329 ($20.8 \pm 6.7\%$) and OCEC ($4.1 \pm 3.3\%$), indicating a highly internally mixed particle population. Pure
330 organic particles only accounted for $2.0 \pm 2.3\%$. The calculation of the margin of error of the mixing
331 state proportions can be found in the SI. The mean diameters of OCEC, OCIn, and OCInEC particles
332 were 0.66, 0.79, and 1.02 μ m, respectively (Fig. S9). This suggests that the internally mixed particles
333 containing three species families tend to be larger than those composed of two species families.

334 **3.3 The effects of particle water uptake on chemical maps**

335 Chemical maps of individual particles under humid conditions (RH = 86%) measured in the
 336 environmental cell were displayed in Fig. 3, and these ROI are identical and matched one by one to
 337 those in Fig. 2. For comparison, the one-to-one particle chemical maps of the same region of interest
 338 under both dry and humid conditions can be found in Fig. S10. It was observed that many particles
 339 tended to be more rounded due to water uptake at high RH, especially for particles with diameters in
 340 the supermicron range (e.g., particles in (ii), (vi), (xi), and (xii) in Fig. 3). If particles take up
 341 significant amounts of water and are homogeneously mixed, they would appear as dominated by
 342 inorganic (colored in cyan) due to absorption of a large amount of water at the carbon pre-edge. In
 343 contrast, most particles remained inhomogeneous and exhibited a core-shell structure under humid
 344 conditions. A possible reason is that the settled RH may not reach the mixing relative humidity (MRH)
 345 of particles, which is defined as a threshold where different phases in an aqueous particle mix into one
 346 homogeneous phase. This MRH usually varies from 84% to over 90% (Li et al., 2021; You et al., 2014;
 347 Zhang et al., 2022).

348 Additionally, around 87% of soot was located at the edge of the humidified particles, with no
 349 obvious location change of soot observed in most particles. A previous study witnessed the
 350 redistribution of soot within phase-separated particles only after the phase mixing process occurred
 351 (Zhang et al., 2022), which is consistent with the phenomenon observed in our study.



352

353 **Figure 3: Chemical maps of individual particles in 12 ROI of sampling substrate under humid conditions**
354 **(RH = 86%) measured in an in-situ environmental cell. Green, cyan, and red color represent dominant**
355 **components of OC, In, and EC, respectively. The scale bar in the upper left image represents 2 μ m and**
356 **applied to all the images.**

357 Comparing size distributions of particle populations under dry (Fig. S8A) and humid conditions
358 (Fig. S8B) reveals that they exhibited similar distribution characteristics. The mean diameter of overall
359 particles at high RH was $0.86 \pm 0.33 \mu\text{m}$, compared with $0.83 \pm 0.30 \mu\text{m}$ under dry conditions. This
360 indicates that the overall size distribution of the humidified particles shifted a little towards larger
361 particles due to water uptake. Specifically, approximately 56.3% of the particles showed an average
362 increase of 14.9% in diameter, while the remaining exhibited an average decrease of 8.2%. Pöhlker et
363 al. (2014) also observed this abnormal phenomenon where some particles decreased in size with
364 increasing RH. They suggested that it could be attributed to the decreasing viscosity and increasing
365 surface tension due to particle water uptake at high RH. This led to larger contact angles between the
366 collected particles and the substrate, causing the particles to “bead up” and therefore reducing their
367 cross-section areas in the view (Pöhlker et al., 2014). In addition, one should note that a small number
368 of particles at the edge of the ROI did not entirely enter the field of view due to the limited observation
369 range, which may slightly affect the quantification of their size.

370 According to the criterion for water uptake by individual particles based on the total oxygen
371 absorbance described in the Sect. 2.3, 41.6% of the particles took up water. As shown in Fig. S11A,
372 OCIn particles were the dominant mixing state type taking up water (76.8%), followed by OCInEC
373 (17.1%). There were also several OCEC (2.4%) and OC (3.7%) particles displayed water uptake.
374 Different particle mixing state types exhibited distinct patterns of hygroscopic behavior. For instance,
375 43.8% of OCIn particles took up water, while 34.1% of OCInEC particles performed the same. This
376 difference may be attributed to varying hygroscopicity of different components. For example, the
377 single hygroscopic parameter (κ) of ammonium nitrate, ammonium sulfate, ammonium hydrogen
378 sulfate, POA, and SOA is 0.58, 0.48, 0.56, 0, and 0.1, respectively (Wu et al., 2016). Based on the
379 AMS data, κ of bulk aerosols during the sampling period (0.25 ± 0.01) was calculated according to
380 κ -Köhler theory (Stokes and Robinson, 1966; Petters and Kreidenweis, 2007), indicating a relatively
381 low hygroscopic capacity of NR-PM₁ during sampling, which could explain why only less than half of
382 the particles exhibited water uptake at such high humidity conditions. In addition, the average diameter

383 of particles taking up water increased from $0.82 \pm 0.33 \mu\text{m}$ to $0.91 \pm 0.36 \mu\text{m}$. The relative frequency
384 distribution and the size-resolved fraction of particles taking up water can be found in Fig. S11B.

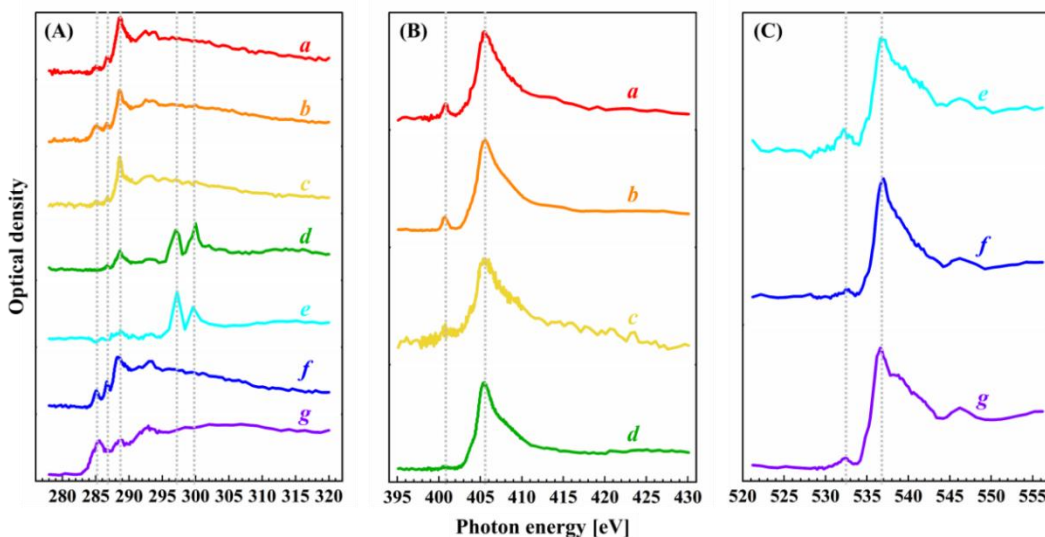
385 **3.4 Chemical composition of ambient submicron particles**

386 NEXAFS spectra with high energy resolution were measured at the C (278 – 320 eV), N (395 –
387 430 eV), and O (525 – 550 eV) K-edges. As shown in Fig. 4A, three notable absorption peaks at the C
388 K-edge were observed at 285.4, 286.7, and 288.6 eV. According to previous literature (Warwick et al.,
389 1998; Moffet et al., 2010a), the peak at 285.4 eV refers to the characteristic transition of sp^2 hybridized
390 carbon ($\text{C } 1\text{s} \rightarrow \pi^*_{\text{R}(\text{C}^*=\text{C})\text{R}}$). The peak at 286.7 eV may result from the transition of ketonic carbonyl (C
391 $1\text{s} \rightarrow \pi^*_{\text{R}(\text{C}^*=\text{O})\text{R}}$), representing ketone and ketone-like compounds. The peak appearing at 288.6 eV
392 represents the characteristic transition of carboxylic carbonyl functional groups ($\text{C } 1\text{s} \rightarrow \pi^*_{\text{R}(\text{C}^*=\text{O})\text{OH}}$),
393 which refers to organic matter and is generally dominant in the outer shell of particles (Moffet et al.,
394 2016; Prather et al., 2013). One should note that there could be extra components in both core and shell
395 in a phase-separated particle with an inorganic-rich core and an organic-rich shell, for example, organic
396 in core or inorganic in shell (Gaikwad et al., 2022). Therefore, the 288.6-eV peak may also be observed
397 in a particle core with relatively low peak intensity. In addition, two other peaks at 296.8 and 299.6 eV
398 were present (see spectra (d) and (e) in Fig. 4A), corresponding to the L_2 - and L_3 -edges of potassium
399 (Moffet et al., 2010a). In our sample, potassium may come from biomass burning processes based on a
400 previous study (Wu et al., 2017).

401 Nitrogen K-edge spectra in Fig. 4B illustrate that ammonium salts were the main nitrogen species
402 in the sample. We observed a broad main peak centered at 405.7 eV, which is the feature of ammonium
403 (Ekimova et al., 2017). A smaller peak was observed at 401.0 eV, which is absorption due to nitrogen
404 gas (N_2) either trapped in the inorganic crystal or formed under X-ray exposure (Latham et al., 2017).
405 Absorption of nitrate (NO_3^-) and nitrite (NO_2^-) commonly have narrow peaks at 405.1 eV and 401.7 eV
406 (Smith et al., 2015), respectively, which were not apparent in our spectra. This is likely because
407 particulate nitrite is below the detection limit, or its peak is masked by the pronounced absorption of
408 ammonium (NH_4^+). The solid ammonium nitrate and sodium nitrate salts could exhibit a peak at around
409 415.0 eV (Smith et al., 2015). However, this was not observed in Fig. 4B. Organic compounds
410 containing nitrogen, such as amino acids, N-heterocyclics, and nitroaromatic compounds, can be
411 abundant in urban aerosol particles due to combustion sources (Yu et al., 2024). They have a large

412 variety of possible peak positions, heights, and widths (Leinweber et al., 2007), making the
 413 identification of these compounds difficult. Although a positive identification of specific organic
 414 nitrides cannot be made, we note that amino acids and 5- or 6-ring heterocycles commonly have narrow
 415 peaks at around 401 eV and broad peaks at 405 eV (Leinweber et al., 2007). We expect that organic
 416 nitrides did contribute to the observed N K-edge spectra, although a targeted study on molecular
 417 identification would be necessary to establish further certainty.

418 Oxygen K-edge spectra in Fig. 4C exhibited a large peak at 536.9 eV, which is a representative
 419 characteristic of sulfate-rich particles (Colberg et al., 2004; Slowik et al., 2011; Mikhailov et al., 2015;
 420 Pöhlker et al., 2014), consistent with the result of AMS. A smaller peak was observed at 532.5 eV,
 421 confirming the presence of ketone, aldehyde, or carboxyl functionalities (Moffet et al., 2011), which
 422 aligns with the results from C K-edge spectra. These compositions tend to take up water under humid
 423 conditions.



424
 425 **Figure 4: NEXAFS spectra for individual particles at (A) carbon (C), (B) nitrogen (N), and (C) oxygen (O)**
 426 **K-edges. In panel (A), peaks were observed at 285.4, 286.7, and 288.6 eV, and two typical peaks appeared at**
 427 **around 296.8 and 299.6 eV in spectra (d) and (e). In panel (B), a main peak appeared at 405.7 eV, and a**
 428 **smaller peak appeared at 410.0 eV. In panel (C), a main peak appeared at 536.9 eV, and a smaller peak was**
 429 **at 532.5 eV. Each small case letter of a spectrum stands for the average result of all the pixels within an**
 430 **individual particle. The same letter in different panels doesn't refer to a same particle.**

431 **4 Conclusions and implications**

432 Particles in the atmosphere usually act as reaction vessels for heterogeneous reactive uptake of
 433 gaseous molecules, and heterogeneous processes play an important part in gas-particle partitioning and

434 secondary aerosol formation (Abbatt et al., 2012; Davidovits et al., 2011; Kolb et al., 2010). However,
435 determining the particle physicochemical properties is crucial but challenging due to the complexity
436 and inhomogeneity of aerosols particles (Barbaray et al., 1979; Zong et al., 2022). So far, there is a lack
437 of study on direct observation of the physicochemical properties of urban aerosols at the single particle
438 level under different conditions, which hinders our understanding of the role of urban particle aerosols
439 in multiphase and heterogeneous chemistry.

440 In this study, we used STXM/NEXAFS spectroscopy combined with an environmental cell to
441 image and quantify the chemical morphology and water uptake behavior of individual submicron
442 particles collected in an urban pollution atmosphere. Results show that most organic compounds were
443 internally mixed with inorganic and/or soot, generally presenting a core-shell structure with an
444 inorganic core and an organic shell. Internally mixed particles composed of organic carbon and
445 inorganic matter dominated the particle population by $73.1 \pm 7.4\%$. At 86%RH, 41.6% of the particles
446 took up water, with OCIn particles making up 76.8% of these hygroscopic particles. The relatively low
447 hygroscopicity of bulk aerosols during the sampling period ($\kappa = 0.25 \pm 0.01$) helps to explain the
448 reason why only less than half of the particles took up water. Besides, the majority of particles still
449 showed a heterogeneous core-shell morphology under humid conditions.

450 This study directly displays the dominant chemical morphology (i.e., core-shell structure) and
451 hygroscopic behavior of individual submicron urban aerosol particles at the microscale. The uptake
452 coefficient onto aerosol particles with different phase states exhibit different patterns as the relative
453 humidity changes (Wang and Lu, 2016). For aqueous particles, the uptake coefficient is closely related
454 to RH (Wang and Lu, 2016). Specifically, when RH is lower than the DRH of the inorganic component,
455 the uptake coefficient increased with the increasing RH. When RH is higher than DRH, the uptake
456 coefficient remains constant. For solid particles, the relationship between the uptake coefficient and RH
457 usually depends on particle species (Wang and Lu, 2016). Results highlight the importance of taking
458 the core-shell structure into consideration for estimating the uptake coefficient and investigating
459 heterogeneous reactions at different humidity, which can improve our comprehension of atmospheric
460 processes of secondary aerosols in typical urban pollution atmospheres.

461 Moreover, previous studies found that the reactive uptake coefficients of N_2O_5 on aqueous sulfuric
462 acid solutions coated with different kinds of organics vary (Cosman and Bertram, 2018; Cosman et al.,
463 2008). The reactive uptake coefficient decreased dramatically for straight-chain surfactants

464 (1-hexadecanol, 1-octadecanol, and stearic acid) by a factor of 17 – 61 depending on the surfactant type.
465 While, the presence of branched surfactant phytanic acid didn't show obvious effect on the reactive
466 uptake coefficient compared to the uncoated solution. These results underlines that the significant
467 impact of organic species on the reactive uptake coefficient. Therefore, on the basis of the high spectral
468 energy resolution of STXM/NEXAFS, it is instrumental to conduct research on the effect of organic
469 molecules and functional groups on heterogeneous reactions in future studies.

470 **ASSOCIATED CONTENT**

471 ***Data availability.*** The data presented in this article can be accessed through the corresponding author
472 Zhijun Wu via E-mail (zhijunwu@pku.edu.cn).

473 ***Author contributions.*** YSZ, PAA, BBW, and JD measured the individual particle sample by
474 STXM/NEXAFS. YSZ, ZJW, YZ, YLG, QC, and SYC carried out the field observation and obtained
475 data. RQM and PAA processed and analyzed data. All authors discussed the results and contributed to
476 the writing of this paper. RQM prepared the manuscript. ZJW, PAA, JC, XRK, MA, and MH further
477 modified and improved the manuscript.

478 ***Competing Interests.*** The authors declare that they have no conflict of interest.

479 ***Acknowledgements.*** We gratefully acknowledge the Swiss Light Source (SLS) for providing a
480 platform for sample measurements. We also thank Benjamin Watts for helping us dealing with
481 technical problems about STXM/NEXAFS.

482 ***Financial support.*** This work has been supported by National Natural Science Foundation of China,
483 International (Regional) Cooperation and Communication Project (NSFC-STINT, China and Sweden;
484 grant No. 42011530121), NSFC (No. 41775133), and the SNSF Swiss Postdoctoral Fellowships (SPF,
485 grant TMPFP2_209830).

486 **References**

487 Abbatt, J. P. D., Lee, A. K. Y., and Thornton, J. A.: Quantifying trace gas uptake to tropospheric
488 aerosol: recent advances and remaining challenges, *Chem. Soc. Rev.*, 41, 6555–6581, DOI:
489 10.1039/c2cs35052a, 2012.

490 Alpert, P. A., Arroyo, P. C., Dou, J., Krieger, U. K., Steimer, S. S., Förster, J.-D., Ditas, F., Pöhlker, C.,
491 Rossignol, S., Passananti, M., Perrier, S., George, C., Shiraiwa, M., Berkemeier, T., Watts, B., and
492 Ammann, M.: Visualizing reaction and diffusion in xanthan gum aerosol particles exposed to
493 ozone, *Phys. Chem. Chem. Phys.*, 21, 20613–20627, DOI: 10.1039/c9cp03731d, 2019.

494 Alpert, P. A., Dou, J., Arroyo, P. C., Schneider, F., Xto, J., Luo, B. P., Peter, T., Huthwelker, T., Borca,
495 C. N., Henzler, K. D., Schaefer, T., Herrmann, H., Raabe, J., Watts, B., Krieger, U. K., and
496 Ammann, M.: Photolytic radical persistence due to anoxia in viscous aerosol particles, *Nat.*
497 *Commun.*, 12, 1769, DOI: 10.1038/s41467-021-21913-x, 2021.

498 Alpert, P. A., Kilthau, W. P., O'Brien, R. E., Moffet, R. C., Gilles, M. K., Wang, B. B., Laskin, A.,
499 Aller, J. Y., and Knopf, D. A.: Ice-nucleating agents in sea spray aerosol identified and quantified
500 with a holistic multimodal freezing model, *Sci. Adv.*, 8, eabq6842, DOI: 10.1126/sciadv.abq6842,
501 2022.

502 Barbaray, B., Contour, J. P., Mouvier, G., Barde, R., Maffiolo, G., and Millancourt, B.: Chemical
503 heterogeneity of aerosol samples as revealed by atomic absorption and x-ray photoelectron
504 spectroscopy, *Environ. Sci. Technol.*, 13, 1530–1532, DOI: 10.1021/es60160a008, 1979.

505 Bond, T. C., Habib, G., and Bergstrom, R. W.: Limitations in the enhancement of visible light
506 absorption due to mixing state, *J. Geophys. Res.: Atmos.*, 111, D20211, DOI:
507 10.1029/2006jd007315, 2006.

508 Bondy, A. L., Bonanno, D., Moffet, R. C., Wang, B. B., Laskin, A., and Ault, A. P.: The diverse
509 chemical mixing state of aerosol particles in the southeastern United States, *Atmos. Chem. Phys.*,
510 18, 12595–12612, DOI: 10.5194/acp-18-12595-2018, 2018.

511 Canagaratna, M. R., Jayne, J. T., Jimenez, J. L., Allan, J. D., Alfarra, M. R., Zhang, Q., Onasch, T. B.,
512 Drewnick, F., Coe, H., Middlebrook, A., Delia, A., Williams, L. R., Trimborn, A. M., Northway,
513 M. J., DeCarlo, P. F., Kolb, C. E., Davidovits, P., and Worsnop, D. R.: Chemical and
514 microphysical characterization of ambient aerosols with the aerodyne aerosol mass spectrometer,
515 *Mass Spectrom. Rev.*, 26, 185–222, DOI: 10.1002/mas.20115, 2007.

516 Chow, J. C., Watson, J. G., Mauderly, J. L., Costa, D.L., Wyzga, R.E., Vedal, S., Hidy, G. M.,
517 Altshuler, S. L., Marrack, D., Heuss, J. M., Wolff, G. T., Pope, C. A., and Dockery, D. W.: Health
518 effects of fine particulate air pollution: Lines that connect, *J. Air Waste Manage. Assoc.*, 56,
519 1368–1380, DOI: 10.1080/10473289.2006.10464545, 2006.

520 Colberg, C. A., Krieger, U. K., and Peter, T.: Morphological investigations of single levitated
521 $\text{H}_2\text{SO}_4/\text{NH}_3/\text{H}_2\text{O}$ aerosol particles during deliquescence/efflorescence experiments, *J. Phys. Chem.*
522 *A.*, 108, 2700–2709, DOI: 10.1021/jp037628r, 2004.

523 Cosman, L. M., and Bertram, A. K.: Reactive Uptake of N_2O_5 on Aqueous H_2SO_4 Solutions Coated
524 with 1-Component and 2-Component Monolayers, *J. Phys. Chem. A.*, 112, 4625–4635, DOI:
525 10.1021/jp8005469, 2008.

526 Cosman, L. M., Knopf, D. A., and Bertram, A. K.: N_2O_5 Reactive Uptake on Aqueous Sulfuric Acid
527 Solutions Coated with Branched and Straight-Chain Insoluble Organic Surfactants, *J. Phys. Chem.*
528 *A.*, 112, 2386–2396, DOI: 10.1021/jp710685r, 2008.

529 Davidovits, P., Kolb, C. E., Williams, L. R., Jayne, J. T., and Worsnop, D. R.: Update 1 of: Mass
530 Accommodation and Chemical Reactions at Gas-Liquid Interfaces, *Chem. Rev.*, 111,
531 PR76–PR109, DOI: 10.1021/cr100360b, 2011.

532 Davies, J. F. and Wilson, K. R.: Chapter 13 - Heterogeneous Reactions in Aerosol, *Physical Chemistry*
533 of Gas-Liquid Interfaces, edited by: Faust, J. A. and House, J. E., Elsevier, the Netherlands,
534 403–433, ISBN: 9780128136416, 2018.

535 Dou, X. D., Yu, S. C., Li, J. L., Sun, Y. H., Song, Z., Yao, N. N., and Li, P. F.: The WRF-CMAQ
536 Simulation of a Complex Pollution Episode with High-Level O_3 and $\text{PM}_{2.5}$ over the North China
537 Plain: Pollution Characteristics and Causes, *Atmosphere*, 15, 198, DOI: 10.3390/atmos15020198,
538 2024.

539 Ekimova, M., Quevedo, W., Szyc, L., Iannuzzi, M., Wernet, P., Odelius, M., and Nibbering, E. T. J.:
540 Aqueous Solvation of Ammonia and Ammonium: Probing Hydrogen Bond Motifs with FT-IR and
541 Soft X-ray Spectroscopy, *J. Am. Chem. Soc.*, 139, 12773–12783, DOI: 10.1021/jacs.7b07207,
542 2017.

543 Eom, H. J., Gupta, D., Li, X., Jung, H. J., Kim, H., and Ro, C. U.: Influence of collecting substrates on
544 the characterization of hygroscopic properties of inorganic aerosol particles, *Anal. Chem.*, 86,
545 2648–2656, DOI: 10.1021/ac4042075, 2014.

546 Fraund, M., Bonanno, D. J., China, S., Pham, D. Q., Veghte, D., Weis, J., Kulkarni, G., Teske, K.,
547 Gilles, M. K., Laskin, A., and Moffet, R. C.: Optical properties and composition of viscous
548 organic particles found in the Southern Great Plains, *Atmos. Chem. Phys.*, 20, 11593–11606, DOI:
549 10.5194/acp-20-11593-2020, 2020.

550 Freedman, M. A.: Phase separation in organic aerosol, *Chem. Soc. Rev.*, 46, 7694–7705, DOI:
551 10.1039/c6cs00783j, 2017.

552 Freedman, M. A.: Liquid-Liquid Phase Separation in Supermicrometer and Submicrometer Aerosol
553 Particles, *Acc. Chem. Res.*, 53, 1102–1110, DOI: 10.1021/acs.accounts.0c00093, 2020.

554 Fröhlich, R., Cubison, M. J., Slowik, J. G., Bukowiecki, N., Prévôt, A. S. H., Baltensperger, U.,
555 Schneider, J., Kimmel, J. R., Gonin, M., Rohner, U., Worsnop, D. R., and Jayne, J. T.: The
556 ToF-ACSM: a portable aerosol chemical speciation monitor with TOFMS detection, *Atmos. Meas.
557 Tech.*, 6, 3225–3241, DOI: 10.5194/amt-6-3225-2013, 2013.

558 Gaikwad, S., Jeong, R., Kim, D., Lee, K., Jang, K.-S., Kim, C., and Song, M.: Microscopic observation
559 of a liquid-liquid-(semi)solid phase in polluted PM_{2.5}, *Front Env. Sci. - Switz*, 10, DOI:
560 10.3389/fenvs.2022.947924, 2022.

561 Gao, J. J., Tian, H. Z., Cheng, K., Lu, L., Zheng, M., Wang, S. X., Hao, J. M., Wang, K., Hua, S. B.,
562 Zhu, C. Y., and Wang, Y.: The variation of chemical characteristics of PM_{2.5} and PM₁₀ and
563 formation causes during two haze pollution events in urban Beijing, China, *Atmos. Environ.*, 107,
564 1–8, DOI: 10.1016/j.atmosenv.2015.02.022, 2015.

565 Gao, J. J., Wang, K., Wang, Y., Liu, S. H., Zhu, C. Y., Hao, J. M., Liu, H. J., Hua, S. B., and Tian, H.
566 Z.: Temporal-spatial characteristics and source apportionment of PM_{2.5} as well as its associated
567 chemical species in the Beijing-Tianjin-Hebei region of China, *Environ. Pollut.*, 233, 714–724,
568 DOI: 10.1016/j.envpol.2017.10.123, 2018.

569 Gao, Y. and Anderson, J. R.: Characteristics of Chinese aerosols determined by individual-particle
570 analysis, *J. Geophys. Res.: Atmos.*, 106, 18037–18045, DOI: 10.1029/2000jd900725, 2001.

571 George, C., Ammann, M., D'Anna, B., Donaldson, D. J., and Nizkorodov, S. A.: Heterogeneous
572 Photochemistry in the Atmosphere, *Chem. Rev.*, 115, 4218–4258, DOI: 10.1021/cr500648z, 2015.

573 George, I. J. and Abbatt, J. P. D.: Heterogeneous oxidation of atmospheric aerosol particles by
574 gas-phase radicalism, *Nat. Chem.*, 2, 713–722, DOI: 10.1038/nchem.806, 2010.

575 Ghorai, S. and Tivanski, A. V.: Hygroscopic Behavior of Individual Submicrometer Particles Studied
576 by X-ray Spectromicroscopy, *Anal. Chem.*, 82, 9289–9298, DOI: 10.1021/ac101797k, 2010.

577 Guo, S., Hu, M., Zamora, M. L., Peng, J. F., Shang, D. J., Zheng, J., Du, Z. F., Wu, Z. J., Shao, M.,
578 Zeng, L. M., Molina, M. J., and Zhang, R. Y.: Elucidating severe urban haze formation in China,
579 *Proc. Natl. Acad. Sci. U. S. A.*, 111, 17373–17378, DOI: 10.1073/pnas.1419604111, 2014.

580 Huang, R. J., Zhang, Y., Bozzetti, C., Ho, K. F., Cao, J. J., Han, Y., Daellenbach, K. R., Slowik, J. G.,
581 Platt, S. M., Canonaco, F., Zotter, P., Wolf, R., Pieber, S. M., Bruns, E. A., Crippa, M., Ciarelli,
582 G., Piazzalunga, A., Schwikowski, M., Abbaszade, G., Schnelle-Kreis, J., Zimmermann, R., An, Z.
583 S., Szidat, S., Baltensperger, U., ElHaddad, I., and Prévôt, A. S. H.: High secondary aerosol
584 contribution to particulate pollution during haze events in China, *Nature*, 514, 218–222, DOI:
585 10.1038/nature13774, 2014.

586 Hopkins, R. J., Tivanski, A. V., Marten, B. D., and Gilles, M. K.: Chemical bonding and structure of
587 black carbon reference materials and individual carbonaceous atmospheric aerosols, *J. Aerosol
588 Sci.*, 38, 573–591, DOI: 10.1016/j.jaerosci.2007.03.009, 2007.

589 Huthwelker, T., Zelenay, V., Birrer, M., Krepelova, A., Raabe, J., Tzvetkov, G., Vernooij, M. G. C.,
590 and Ammann, M.: An in situ cell to study phase transitions in individual aerosol particles on a
591 substrate using scanning transmission x-ray microspectroscopy, *Rev. Sci. Instrum.*, 81, 113706,
592 DOI: 10.1063/1.3494604, 2010.

593 Jahl, L. G., Bowers, B. B., Jahn, L. G., Thornton, J. A., and Sullivan, R. C.: Response of the reaction
594 probability of N_2O_5 with authentic biomass-burning aerosol to high relative humidity, *ACS Earth
595 Space Chem.*, 5, 2587–2598, DOI: 10.1021/acsearthspacechem.1c00227, 2021.

596 Jahn, L. G., Jahl, L. G., Bowers, B. B., and Sullivan, R. C.: Morphology of organic carbon coatings on
597 biomass-burning particles and their role in reactive gas uptake, *ACS Earth Space Chem.*, 5,
598 2184–2195, DOI: 10.1021/acsearthspacechem.1c00237, 2021.

599 Knopf, D. A., Wang, P. W., Wong, B. Y., Tomlin, J. M., Veghte, D. P., Lata, N. N., China, S., Laskin,
600 A., Moffet, R. C., Aller, J. Y., Marcus, M. A., and Wang, J.: Physicochemical characterization of
601 free troposphere and marine boundary layer ice-nucleating particles collected by aircraft in the
602 eastern North Atlantic, *Atmos. Chem. Phys.*, 23, 8659–8681, DOI: 10.5194/acp-23-8659-2023,
603 2023.

604 Kolb, C. E., Cox, R. A., Abbatt, J. P. D., Ammann, M., Davis, E. J., Donaldson, D. J., Garrett, B. C.,
605 George, C., Griffiths, P. T., Hanson, D. R., Kulmala, M., McFiggans, G., Pöschl, U., Riipinen, I.,
606 Rossi, M. J., Rudich, Y., Wagner, P. E., Winkler, P. M., Worsnop, D. R., and O'Dowd, C. D.: An
607 overview of current issues in the uptake of atmospheric trace gases by aerosols and clouds, *Atmos.*
608 *Chem. Phys.*, 10, 10561–10605, DOI: 10.5194/acp-10-10561-2010, 2010.

609 Krieger, U. K., Marcolli, C., and Reid, J. P.: Exploring the complexity of aerosol particle properties
610 and processes using single particle techniques, *Chem. Soc. Rev.*, 41, 6631–6662, DOI:
611 10.1039/c2cs35082c, 2012.

612 Lata, N. N., Zhang, B., Schum, S., Mazzoleni, L., Brimberry, R., Marcus, M. A., Cantrell, W. H.,
613 Fialho, P., Mazzoleni, C., and China, S.: Aerosol Composition, Mixing State, and Phase State of
614 Free Tropospheric Particles and Their Role in Ice Cloud Formation, *ACS Earth Space Chem.*, 5,
615 3499–3510, DOI: 10.1021/acsearthspacechem.1c00315, 2021.

616 Latham, K. G., Simone, M. I., Dose, W. M., Allen, J. A., and Donne, S. W.: Synchrotron based
617 NEXAFS study on nitrogen doped hydrothermal carbon: Insights into surface functionalities and
618 formation mechanisms, *Carbon*, 114, 566–578, DOI: 10.1016/j.carbon.2016.12.057, 2017.

619 Lei, L., Zhou, W., Chen, C., He, Y., Li, Z. J., Sun, J. X., Tang, X., Fu, P. Q., Wang, Z. F., and Sun, Y.
620 L.: Long-term characterization of aerosol chemistry in cold season from 2013 to 2020 in Beijing,
621 China, *Environ. Pollut.*, 268, 115952, DOI: 10.1016/j.envpol.2020.115952, 2021.

622 Leinweber, P., Kruse, J., Walley, F. L., Gillespie, A., Eckhardt, K. U., Blyth, R. I. R., and Regier, T.:
623 Nitrogen K-edge XANES - An overview of reference compounds used to identify 'unknown'
624 organic nitrogen in environmental samples, *J. Synchrotron Radiat.*, 14, 500–511, DOI:
625 10.1107/s0909049507042513, 2007.

626 Li, W. J., Shao, L. Y., Zhang, D. Z., Ro, C. U., Hu, M., Bi, X. H., Geng, H., Matsuki, A., Niu, H. Y.,
627 and Chen, J. M.: A review of single aerosol particle studies in the atmosphere of East Asia:
628 morphology, mixing state, source, and heterogeneous reactions, *J. Cleaner Prod.*, 112, 1330–1349,
629 DOI: 10.1016/j.jclepro.2015.04.050, 2016.

630 Li, W. J., Liu, L., Zhang, J., Xu, L., Wang, Y. Y., Sun, Y. L., and Shi, Z. B.: Microscopic Evidence for
631 Phase Separation of Organic Species and Inorganic Salts in Fine Ambient Aerosol Particles,
632 *Environ. Sci. Technol.*, 55, 2234–2242, DOI: 10.1021/acs.est.0c02333, 2021.

633 Li, Y. J., Sun, Y. L., Zhang, Q., Li, X., Li, M., Zhou, Z., and Chan, C. K.: Real-time chemical
634 characterization of atmospheric particulate matter in China: A review, *Atmos. Environ.*, 158,
635 270–304, DOI: 10.1016/j.atmosenv.2017.02.027, 2017.

636 Liu, Z. R., Gao, W. K., Yu, Y. C., Hu, B., Xin, J. Y., Sun, Y., Wang, L. L., Wang, G. H., Bi, X. H.,
637 Zhang, G. H., Xu, H. H., Cong, Z. Y., He, J., Xu, J. S., and Wang, Y. S.: Characteristics of PM_{2.5}
638 mass concentrations and chemical species in urban and background areas of China: emerging
639 results from the CARE-China network, *Atmos. Chem. Phys.*, 18, 8849–8871, DOI:
640 10.5194/acp-18-8849-2018, 2018.

641 Martin, S. T.: Phase transitions of aqueous atmospheric particles, *Chem. Rev.*, 100, 3403–3453, DOI:
642 10.1021/cr990034t, 2001.

643 McCormick, R. A. and Ludwig, J. H.: Climate Modification by Atmospheric Aerosols, *Science*, 156,
644 1358–1359, DOI: 10.1126/science.156.3780.1358, 1967.

645 Middlebrook, A. M., Bahreini, R., Jimenez, J. L., and Canagaratna, M. R.: Evaluation of
646 Composition-Dependent Collection Efficiencies for the Aerodyne Aerosol Mass Spectrometer
647 using Field Data, *Aerosol Sci. Technol.*, 46, 258–271, DOI: 10.1080/02786826.2011.620041,
648 2012.

649 Mikhailov, E. F., Mironov, G. N., Pöhlker, C., Chi, X., Krüger, M. L., Shiraiwa, M., Förster, J. D.,
650 Pöschl, U., Vlasenko, S. S., Ryshkevich, T. I., Weigand, M., Kilcoyne, A. L. D., and Andreae, M.
651 O.: Chemical composition, microstructure, and hygroscopic properties of aerosol particles at the
652 Zotino Tall Tower Observatory (ZOTTO), Siberia, during a summer campaign, *Atmos. Chem.*
653 *Phys.*, 15, 8847–8869, DOI: 10.5194/acp-15-8847-2015, 2015.

654 Moffet, R. C., Henn, T., Laskin, A., and Gilles, M. K.: Automated Chemical Analysis of Internally
655 Mixed Aerosol Particles Using X-ray Spectromicroscopy at the Carbon K-Edge, *Anal. Chem.*, 82,
656 7906–7914, DOI: 10.1021/ac1012909, 2010a.

657 Moffet, R. C., Henn, T. R., Tivanski, A. V., Hopkins, R. J., Desyaterik, Y., Kilcoyne, A. L. D.,
658 Tyliszczak, T., Fast, J., Barnard, J., Shutthanandan, V., Cliff, S. S., Perry, K. D., Laskin, A., and
659 Gilles, M. K.: Microscopic characterization of carbonaceous aerosol particle aging in the outflow
660 from Mexico City, *Atmos. Chem. Phys.*, 10, 961–976, DOI: 10.5194/acp-10-961-2010, 2010b.

661 Moffet, R. C., Tivanski A. V., and Gilles M. K.: Scanning Transmission X-ray Microscopy
662 Applications in Atmospheric Aerosol Research, Fundamentals and Applications in Aerosol

663 Spectroscopy, edited by: Signorell, R., and Reid, J. P., CRC Press, the U.S., 419–462, ISBN:
664 9781420085617, 2011.

665 Moffet, R. C., Rödel, T. C., Kelly, S. T., Yu, X. Y., Carroll, G. T., Fast, J., Zaveri, R. A., Laskin, A.,
666 and Gilles, M. K.: Spectro-microscopic measurements of carbonaceous aerosol aging in Central
667 California, *Atmos. Chem. Phys.*, 13, 10445–10459, DOI: 10.5194/acp-13-10445-2013, 2013.

668 Moffet, R. C., O'Brien, R. E., Alpert, P. A., Kelly, S. T., Pham, D. Q., Gilles, M. K., Knopf, D. A., and
669 Laskin, A.: Morphology and mixing of black carbon particles collected in central California
670 during the CARES field study, *Atmos. Chem. Phys.*, 16, 14515–14525, DOI:
671 10.5194/acp-16-14515-2016, 2016.

672 Mori, T., Goto-Azuma, K., Kondo, Y., Ogawa-Tsukagawa, Y., Miura, K., Hirabayashi, M., Oshima, N.,
673 Koike, M., Kupiainen, K., Moteki, N., Ohata, S., Sinha, P. R., Sugiura, K., Aoki, T., Schneebeli,
674 M., Steffen, K., Sato, A., Tsushima, A., Makarov, V., Omiya, S., Sugimoto, A., Takano, S., and
675 Nagatsuka, N.: Black carbon and inorganic aerosols in Arctic snowpack, *JGR. Atmos.*, 124 (23),
676 13325–13356, DOI: 10.1029/2019JD030623, 2019.

677 Mori, T., Moteki, N., Ohata, S., Koike, M., Goto-Azuma, K., Miyazaki, Y., and Kondo, Y.: Improved
678 technique for measuring the size distribution of black carbon particles in liquid water, *Aerosol Sci.
679 Tech.*, 50 (3), 242–254, DOI: 10.1080/02786826.2016.1147644, 2016.

680 Noll, K. E., Mueller, P. K., and Imada, M.: Visibility and aerosol concentration in urban air, *Atmos.
681 Environ.*, 2, 465–475, DOI: 10.1016/0004-6981(68)90040-1, 1968.

682 O'Brien, R. E., Neu, A., Epstein, S. A., Macmillan, A. C., Wang, B. B., Kelly, S. T., Nizkorodov, S. A.,
683 Laskin, A., Moffet, R. C., and Gilles, M. K.: Physical properties of ambient and
684 laboratory-generated secondary organic aerosol, *Geophys. Res. Lett.*, 41, 4347–4353, DOI:
685 org/10.1002/2014GL060219, 2014.

686 O'Brien, R. E., Wang, B. B., Kelly, S. T., Lundt, N., You, Y., Bertram, A. K., Leone, S. R., Laskin, A.,
687 and Gilles, M. K.: Liquid-Liquid Phase Separation in Aerosol Particles: Imaging at the Nanometer
688 Scale, *Environ. Sci. Technol.*, 49, 4995–5002, DOI: 10.1021/acs.est.5b00062, 2015.

689 Peng, C., Chen, L. X. D., and Tang, M. J.: A database for deliquescence and efflorescence relative
690 humidities of compounds with atmospheric relevance, *Fundam. Res.*, 2, 578–587, DOI:
691 10.1016/j.fmre.2021.11.021, 2022.

692 Penner, J. E. and Novakov, T.: Carbonaceous particles in the atmosphere: A historical perspective to
693 the Fifth International Conference on Carbonaceous Particles in the Atmosphere, *J. Geophys. Res.:*
694 *Atmos.*, 101, 19373–19378, DOI: 10.1029/96JD01175, 1996.

695 Petters, M. D. and Kreidenweis, S. M.: A single parameter representation of hygroscopic growth and
696 cloud condensation nucleus activity, *Atmos. Chem. Phys.*, 7, 1961–1971, DOI:
697 10.5194/acp-7-1961-2007, 2007.

698 Piens, D. S., Kelly, S. T., Harder, T. H., Petters, M. D., O'Brien, R. E., Wang, B. B., Teske, K., Dowell,
699 P., Laskin, A., and Gilles, M. K.: Measuring Mass-Based Hygroscopicity of Atmospheric Particles
700 through in Situ Imaging, *Environ. Sci. Technol.*, 50, 5172–5180, DOI: 10.1021/acs.est.6b00793,
701 2016.

702 Pöhlker, C., Saturno, J., Krüger, M. L., Förster, J. D., Weigand, M., Wiedemann, K. T., Bechtel, M.,
703 Artaxo, P., and Andreae, M. O.: Efflorescence upon humidification? X-ray microspectroscopic in
704 situ observation of changes in aerosol microstructure and phase state upon hydration, *Geophys.*
705 *Res. Lett.*, 41, 3681–3689, DOI: 10.1002/2014gl059409, 2014.

706 Prather, K. A., Bertram, T. H., Grassian, V. H., Deane, G. B., Stokes, M. D., DeMott, P. J., Aluwihare,
707 L. I., Palenik, B. P., Azam, F., Seinfeld, J. H., Moffet, R. C., Molina, M. J., Cappa, C. D., Geiger,
708 F. M., Roberts, G. C., Russell, L. M., Ault, A. P., Baltrusaitis, J., Collins, D. B., Corrigan, C. E.,
709 Cuadra-Rodriguez, L. A., Ebben, C. J., Forestieri, S. D., Guasco, T. L., Hersey, S. P., Kim, M. J.,
710 Lambert, W. F., Modini, R. L., Mui, W., Pedler, B. E., Ruppel, M. J., Ryder, O. S., Schoepp, N.
711 G., Sullivan, R. C., and Zhao, D. F.: Bringing the ocean into the laboratory to probe the chemical
712 complexity of sea spray aerosol, *Proc. Natl. Acad. Sci. U. S. A.*, 110, 7550–7555, DOI:
713 10.1073/pnas.1300262110, 2013.

714 Raabe, J., Tzvetkov, G., Flechsig, U., Böge, M., Jaggi, A., Sarafimov, B., Vernooij, M. G. C.,
715 Huthwelker, T., Ade, H., Kilcoyne, D., Tyliszczak, T., Fink, R. H., and Quitmann, C.: PolLux: A
716 new facility for soft x-ray spectromicroscopy at the Swiss Light Source, *Rev. Sci. Instrum.*, 79,
717 113704, DOI: 10.1063/1.3021472, 2008.

718 Rasool, S. I. and Schneider, S. H.: Atmospheric Carbon Dioxide and Aerosols: Effects of Large
719 Increases on Global Climate, *Science*, 173, 138–141, DOI: 10.1126/science.173.3992.138, 1971.

720 Resch, J., Wolfer, K., Barth, A., and Kalberer, M.: Effects of storage conditions on the molecular-level
721 composition of organic aerosol particles, *Atmos. Chem. Phys.*, 23, 9161–9171, DOI:

722 10.5194/acp-23-9161-2023, 2023.

723 Reynolds, R. S. and Wilson, K. R.: Unraveling the Meaning of Effective Uptake Coefficients in
724 Multiphase and Aerosol Chemistry, *Acc. Chem. Res.*, 58, 366–374, DOI:
725 10.1021/acs.accounts.4c00662, 2025.

726 Riemer, N., Ault, A. P., West, M., Craig, R. L., and Curtis, J. H.: Aerosol Mixing State: Measurements,
727 Modeling, and Impacts, *Rev. Geophys.*, 57, 187–249, DOI: 10.1029/2018rg000615, 2019.

728 Shao, L. Y., Liu, P. J., Jones, T., Yang, S. S., Wang, W. H., Zhang, D. Z., Li, Y. W., Yang, C.-X., Xing,
729 J. P., Hou, C., Zhang, M. Y., Feng, X. L., Li, W. J., and BéruBé K.: A review of atmospheric
730 individual particle analyses: Methodologies and applications in environmental research,
731 *Gondwana Res.*, 110, 347–369, DOI: 10.1016/j.gr.2022.01.007, 2022.

732 Shen, X. J., Sun, J. Y., Zhang, X. Y., Zhang, Y. M., Zhong, J. T., Wang, X., Wang, Y. Q., and Xia, C.:
733 Variations in submicron aerosol liquid water content and the contribution of chemical components
734 during heavy aerosol pollution episodes in winter in Beijing, *Sci. Total Environ.*, 693, 133521,
735 DOI: 10.1016/j.scitotenv.2019.07.327, 2019.

736 Slowik, J. G., Cziczo, D. J., and Abbatt, J. P. D.: Analysis of cloud condensation nuclei composition
737 and growth kinetics using a pumped counterflow virtual impactor and aerosol mass spectrometer,
738 *Atmos. Meas. Tech.*, 4, 1677–1688, DOI: 10.5194/amt-4-1677-2011, 2011.

739 Smith, J. W., Lam, R. K., Shih, O., Rizzuto, A. M., Prendergast, D., and Saykally, R. J.: Properties of
740 aqueous nitrate and nitrite from x-ray absorption spectroscopy, *J. Chem. Phys.*, 143, 084503, DOI:
741 10.1063/1.4928867, 2015.

742 Song, M., Jeong, R., Kim, D., Qiu, Y. T., Meng, X. X. Y., Wu, Z. J., Zuend, A., Ha, Y., Kim, C., Kim,
743 H., Gaikwad, S., Jang, K. S., Lee, J. Y., and Ahn, J.: Comparison of Phase States of PM_{2.5} over
744 Megacities, Seoul and Beijing, and Their Implications on Particle Size Distribution, *Environ. Sci.*
745 *Technol.*, 56, 17581–17590, DOI: 10.1021/acs.est.2c06377, 2022.

746 Stokes, R. H. and Robinson, R. A.: Interactions in aqueous nonelectrolyte solutions. I. Solute-solvent
747 equilibria, *J. Phys. Chem.*, 70, 2126–2131, DOI: 10.1021/j100879a010, 1966.

748 Su, H., Cheng, Y. F., and Pöschl, U.: New Multiphase Chemical Processes Influencing Atmospheric
749 Aerosols, Air Quality, and Climate in the Anthropocene, *Acc. Chem. Res.*, 53, 2034–2043, DOI:
750 10.1021/acs.accounts.0c00246, 2020.

751 Sun, Y. L., Wang, Z. F., Fu, P. Q., Yang, T., Jiang, Q., Dong, H. B., Li, J., and Jia, J. J.: Aerosol
752 composition, sources and processes during wintertime in Beijing, China, *Atmos. Chem. Phys.*, 13,
753 4577–4592, DOI: 10.5194/acp-13-4577-2013, 2013.

754 Tang, L. Z., Shang, D. J., Fang, X., Wu, Z. J., Qiu, Y. T., Chen, S. Y., Li, X., Zeng, L. M., Guo, S., and
755 Hu, M.: More Significant Impacts From New Particle Formation on Haze Formation During
756 COVID-19 Lockdown, *Geophys. Res. Lett.*, 48, e2020GL091591, DOI: 10.1029/2020gl091591,
757 2021.

758 Tang, M. J., Cziczo, D. J., and Grassian, V. H.: Interactions of Water with Mineral Dust Aerosol:
759 Water Adsorption, Hygroscopicity, Cloud Condensation, and Ice Nucleation, *Chem. Rev.*, 116,
760 4205–4259, DOI: 10.1021/acs.chemrev.5b00529, 2016.

761 Tang, M. J., Chan, C. K., Li, Y. J., Su, H., Ma, Q. X., Wu, Z. J., Zhang, G. H., Wang, Z., Ge, M. F., Hu,
762 M., He, H., and Wang, X. M.: A review of experimental techniques for aerosol hygroscopicity
763 studies, *Atmos. Chem. Phys.*, 19, 12631–12686, DOI: 10.5194/acp-19-12631-2019, 2019.

764 Tomlin, J. M., Weis, J., Veghte, D. P., China, S., Fraund, M., He, Q., Reicher, N., Li, C., Jankowski, K.
765 A., Rivera-Adorno, F. A., Morales, A. C., Rudich, Y., Moffet, R. C., Gilles, M. K., and Laskin, A.:
766 Chemical composition and morphological analysis of atmospheric particles from an intensive
767 bonfire burning festival, *Environ. Sci.: Atmos.*, 2, 616–633, DOI: 10.1039/d2ea00037g, 2022.

768 Ueda, S., Ohata, S., Iizuka, Y., Seki, O., Matoba, S., Matsui, H., Koike, M., and Kondo, Y.: Evaluation
769 of sample storage methods for single particle analyses of black carbon in snow and ice: Merits and
770 risks of glass and plastic vials for melted sample storage, *Aerosol Sci. Tech.*, 1–16, DOI:
771 10.1080/02786826.2025.2542900, 2025.

772 Ulbrich, I. M., Canagaratna, M. R., Zhang, Q., Worsnop, D. R., and Jimenez, J. L.: Interpretation of
773 organic components from Positive Matrix Factorization of aerosol mass spectrometric data, *Atmos.*
774 *Chem. Phys.*, 9, 2891–2918, DOI: 10.5194/acp-9-2891-2009, 2009.

775 Wagner, N. L., Riedel, T. P., Young, C. J., Bahreini, R., Brock, C. A., Dubé, W. P., Kim, S.,
776 Middlebrook, A. M., Öztürk, F., Roberts, J. M., Russo, R., Sive, B., Swarthout, R., Thornton, J. A.,
777 VandenBoer, T. C., Zhou, Y., and Brown, S. S.: N_2O_5 uptake coefficients and nocturnal NO_2
778 removal rates determined from ambient wintertime measurements, *J. Geophys. Res.: Atmos.*, 118,
779 9331–9350, DOI: 10.1002/jgrd.50653, 2013.

780 Wang, H. C., and Lu, K. D.: Determination and Parameterization of the Heterogeneous Uptake
781 Coefficient of Dinitrogen Pentoxide (N_2O_5), *Prog. Chem.*, 28, 917–933, DOI: 10.7536/PC151225,
782 2016.

783 Wang, Y. C., Chen, J., Wang, Q. Y., Qin, Q. D., Ye, J. H., Han, Y. M., Li, L., Zhen, W., Zhi, Q., Zhang,
784 Y. X., and Cao, J. J.: Increased secondary aerosol contribution and possible processing on polluted
785 winter days in China, *Environ. Int.*, 127, 78–84, DOI: 10.1016/j.envint.2019.03.021, 2019.

786 Wang, Y. S., Yao, L., Wang, L. L., Liu, Z. R., Ji, D. S., Tang, G. Q., Zhang, J. K., Sun, Y., Hu, B., and
787 Xin, J. Y.: Mechanism for the formation of the January 2013 heavy haze pollution episode over
788 central and eastern China, *Sci. China: Earth Sci.*, 57, 14–25, DOI: 10.1007/s11430-013-4773-4,
789 2014.

790 Warwick, T., Franck, K., Kortright, J. B., Meigs, G., Moronne, M., Myneni, S., Rotenberg, E., Seal, S.,
791 Steele, W. F., Ade, H., Garcia, A., Cerasari, S., Delinger, J., Hayakawa, S., Hitchcock, A. P.,
792 Tyliszczak, T., Kikuma, J., Rightor, E. G., Shin, H. J., and Tonner, B. P.: A scanning transmission
793 x-ray microscope for materials science spectromicroscopy at the advanced light source, *Rev. Sci.*
794 *Instrum.*, 69, 2964–2973, DOI: 10.1063/1.1149041, 1998.

795 Wendl, I. A., Menking, J. A., Färber, R., Gysel, M., Kaspari, S. D., Laborde, M. J. G., and
796 Schwikowski, M.: Optimized method for black carbon analysis in ice and snow using the single
797 particle soot photometer, *Atmos. Meas. Tech.*, 7 (8), 2667–2681, DOI: 10.5194/amt-7-2667-2014,
798 2014.

799 Wu, L. and Ro, C. U.: Aerosol Hygroscopicity on A Single Particle Level Using Microscopic and
800 Spectroscopic Techniques: A Review, *Asian J. Atmos. Environ.*, 14, 177–209, DOI:
801 10.5572/ajae.2020.14.3.177, 2020.

802 Wu, Z. J., Hu, M., Liu, S., Wehner, B., Bauer, S., Maßling, A., Wiedensohler, A., Petäjä, T., Dal Maso,
803 M., and Kulmala, M.: New particle formation in Beijing, China: Statistical analysis of a 1-year
804 data set, *J. Geophys. Res.: Atmos.*, 112, D0920, DOI: 10.1029/2006jd007406, 2007.

805 Wu, Z. J., Zheng, J., Shang, D. J., Du, Z. F., Wu, Y. S., Zeng, L. M., Wiedensohler, A., and Hu, M.:
806 Particle hygroscopicity and its link to chemical composition in the urban atmosphere of Beijing,
807 China, during summertime, *Atmos. Chem. Phys.*, 16, 1123–1138, DOI:
808 10.5194/acp-16-1123-2016, 2016.

809 Wu, Z. J., Zheng, J., Wang, Y., Shang, D. J., Du, Z. F., Zhang, Y. H., and Hu, M.: Chemical and
810 physical properties of biomass burning aerosols and their CCN activity: A case study in Beijing,
811 China, *Sci. Total Environ.*, 579, 1260–1268, DOI: 10.1016/j.scitotenv.2016.11.112, 2017.

812 Xiao, Z. M., Xu, H., Gao, J. Y., Cai, Z. Y., Bi, W. K., Li, P., Yang, N., Deng, X. W., Ji, Y. F.:
813 Characteristics and Sources of PM_{2.5}-O₃ Compound Pollution in Tianjin, *Environmental Science*
814 (Chinese), 43, 1140–1150, DOI: 10.13227/j.hjkx.202108164, 2022.

815 You, Y., Renbaum-Wolff, L., Carreras-Sospedra, M., Hanna, S. J., Hiranuma, N., Kamal, S., Smith, M.
816 L., Zhang, X. L., Weber, R. J., Shilling, J. E., Dabdub, D., Martin, S. T., and Bertram, A. K.:
817 Images reveal that atmospheric particles can undergo liquid-liquid phase separations, *Proc. Natl.
818 Acad. Sci. U. S. A.*, 109, 13188–13193, DOI: 10.1073/pnas.1206414109, 2012.

819 You, Y., Renbaum-Wolff, L., and Bertram, A. K.: Liquid-liquid phase separation in particles
820 containing organics mixed with ammonium sulfate, ammonium bisulfate, ammonium nitrate or
821 sodium chloride, *Atmos. Chem. Phys.*, 13, 11723–11734, DOI: 10.5194/acp-13-11723-2013,
822 2013.

823 You, Y., Smith, M. L., Song, M. J., Martin, S. T., and Bertram, A. K.: Liquid–liquid phase separation
824 in atmospherically relevant particles consisting of organic species and inorganic salts, *Int. Rev.
825 Phys. Chem.*, 33, 43–77, DOI: 10.1080/0144235x.2014.890786, 2014.

826 Yu, X., Li, Q. F., Liao, K. Z., Li, Y. M., Wang, X. M., Zhou, Y., Liang, Y. M., and Yu, J. Z.: New
827 measurements reveal a large contribution of nitrogenous molecules to ambient organic aerosol, *npj
828 Clim. Atmos. Sci.*, 7, 72, DOI: 10.1038/s41612-024-00620-6, 2024.

829 Zelenay, V., Ammann, M., Křepelová, A., Birrer, M., Tzvetkov, G., Vernooij, M. G. C., Raabe, J., and
830 Huthwelker, T.: Direct observation of water uptake and release in individual submicrometer sized
831 ammonium sulfate and ammonium sulfate/adipic acid particles using X-ray microspectroscopy, *J.
832 Aerosol Sci.*, 42, 38–51, DOI: 10.1016/j.jaerosci.2010.11.001, 2011a.

833 Zelenay, V., Huthwelker, T., Krepelová, A., Rudich, Y., and Ammann, M.: Humidity driven nanoscale
834 chemical separation in complex organic matter, *Environ. Chem.*, 8, 450–460, DOI:
835 10.1071/en11047, 2011b.

836 Zhang, J., Wang, Y. Y., Teng, X. M., Liu, L., Xu, Y. S., Ren, L. H., Shi, Z. B., Zhang, Y., Jiang, J. K.,
837 Liu, D. T., Hu, M., Shao, L. Y., Chen, J. M., Martin, S. T., Zhang, X. Y., and Li, W. J.:

838 Liquid-liquid phase separation reduces radiative absorption by aged black carbon aerosols,
839 *Commun. Earth Environ.*, 3, 128, DOI: 10.1038/s43247-022-00462-1, 2022.

840 Zhao, X. J., Zhao, P. S., Xu, J., Meng, W., Pu, W. W., Dong, F., He, D., and Shi, Q. F.: Analysis of a
841 winter regional haze event and its formation mechanism in the North China Plain, *Atmos. Chem.*
842 *Phys.*, 13, 5685–5696, DOI: 10.5194/acp-13-5685-2013, 2013.

843 Zheng, Y., Cheng, X., Liao, K. R., Li, Y. W., Li, Y. J., Huang, R.-J., Hu, W. W., Liu, Y., Zhu, T., Chen,
844 S. Y., Zeng, L. M., Worsnop, D. R., and Chen, Q.: Characterization of anthropogenic organic
845 aerosols by TOF-ACSM with the new capture vaporizer, *Atmos. Meas. Tech.*, 13, 2457–2472,
846 DOI: 10.5194/amt-13-2457-2020, 2020.

847 Zheng, Y., Miao, R. Q., Zhang, Q., Li, Y. W., Cheng, X., Liao, K. R., Koenig, T. K., Ge, Y. L., Tang,
848 L. Z., Shang, D. J., Hu, M., Chen, S. Y., and Chen, Q.: Secondary Formation of Submicron and
849 Supermicron Organic and Inorganic Aerosols in a Highly Polluted Urban Area, *J. Geophys. Res.:
850 Atmos.*, 128, e2022JD037865, DOI: 10.1029/2022jd037865, 2023.

851 Ziemann, P. J. and Atkinson, R.: Kinetics, products, and mechanisms of secondary organic aerosol
852 formation, *Chem. Soc. Rev.*, 41, 6582–6605, DOI: 10.1039/c2cs35122f, 2012.

853 Zong, T. M., Wang, H. C., Wu, Z. J., Lu, K. D., Wang, Y., Zhu, Y. S., Shang, D. J., Fang, X., Huang,
854 X. F., He, L. Y., Ma, N., Gröss, J., Huang, S., Guo, S., Zeng, L. M., Herrmann, H., Wiedensohler,
855 A., Zhang, Y. H., and Hu, M.: Particle hygroscopicity inhomogeneity and its impact on reactive
856 uptake, *Sci. Total Environ.*, 811, 151364, DOI: 10.1016/j.scitotenv.2021.151364, 2022.